Supporting Information for

Unraveling the Impact of Heterogeneity and Morphology on Light Absorption Enhancement of Black Carbon-Containing Particles

Jing Wei[1], Jin-Mei Ding[2], Yao Song[1], Xiao-Yuan Wang[2], Xiang-Yu Pei[1], Sheng-Chen Xu[2], Fei Zhang[1], Zheng-Ning Xu[1], Xu-Dong Tian[2], Bing-Ye Xu[2], Zhi-Bin Wang[1,3]

[1] State Key Laboratory of Soil Pollution Control and Safety, Zhejiang Provincial Key Laboratory of Organic Pollution Process and Control, College of Environmental and Resource Sciences, Zhejiang University, Hangzhou 310058, China

[2] Ecological and Environmental Monitoring Center of Zhejiang Province, Hangzhou 310012, China

[3] ZJU-Hangzhou Global Scientific and Technological Innovation Center, Zhejiang University, Hangzhou 311200, China

Correspondence: Bing-Ye Xu (xubingye@zjemc.org.cn) and Zhi-Bin Wang (wangzhibin@zju.edu.cn)

Contents of this file

Introduction

Text S1. Correction of DMA-SP2 data

Table S1. The M_R determination range of "transition-state" BC-containing particles at different periods

Figure S1. Schematic of the sampling system. The dotted line represents the SP2 sample flow, and the red line represents the CPMA-SP2 tandem system sample flow.

Figure S2. The number concentration measured by SP2 and CPC after DMA classification of size-resolved Aquadag aerosols (a). (b) showed the calibration factor for scattering channel before and after campaign. (c) and (d) display the correlation between incandescence peak height and BC particle mass at broadband high-gain and low-gain channel, respectively.

Figure S3. The scattering coefficient, absorption coefficient and extinction coefficient of particles were measured by CAPS at wavelength of 445 nm, 530 nm and 630 nm.

Figure S4. Comparisons of the scattering coefficients measured by CAPS at wavelengths of 445 nm, 530 nm, and 630 nm, and by the nephelometer at wavelengths of 450 nm, 525 nm, and 635 nm.

Figure S5. The scattering coefficients measured by CAPS (a) and the Nephelometer (b) are compared with those modeled using Mie theory.

Figure S6. The relationship between MAC and bulk-averaged M_R at λ=630 nm is shown, with fitted lines and their associated 90th confidence intervals. The extrapolated MAC value for pure BC (MAC_{BC_core}) at a bulk-averaged M_R of 0 is 9.08 m^2 g^{-1} (630 nm), with uncertainties representing the 90th confidence level. The grey dots were the residual from the fits.

Figure S7. The time series of BC concentrations, bulk-averaged M_R, and the measured E_{abs}, and the chemical components including organic, nitrate, sulfate, ammonium, chloride and the relatively humidity (RH). Shaded regions indicate different cases: light yellow for Case 1, blue-green for Case 2, and gray for Case 3. The top horizontal bar indicates the air mass origins throughout the observation period; the associated air mass directions are illustrated in Fig. S8.

Figure S8. Air mass backward trajectory by during the observation period.

Figure S9. The proportions of externally mixed, transitional, and internally mixed BC-containing particles during different cases.

Figure S10. Multiple charging diagnostics in the tandem CPMA-SP2 system. (a) presents the number distribution of M_c-M_p before removing the BC-containing particles affected by multiple charging. (b) displays the number distribution of M_c-M_p after removing the BC-containing particles affected by multiple charging. (c) and (d) demonstrate the selection approach for single-charged BC-containing particles at different M_p, exemplified by M_p =2.97 fg and M_p =9.38fg.

Figure S11. Mass-dependent charging efficiency of singly charged BC-containing particles and the associated tubing loss.

Text S1. Correction of DMA-SP2 data

(1) Correction of delay time. Aerosols are passed through the CPMA for mass selection before being measured by the SP2. Due to differences in tubing length and the response times of the instruments or computers, there exists a time lag between the CPMA and SP2 measurements, which affects the accuracy of their mass correspondence. In addition, the CPMA requires different rotational speeds to select particles of different masses, which leads to a certain response delay during mass switching. Since the time required for rotational speed switching varies between different mass settings, it is difficult to accurately correct for this delay. Therefore, in the data processing, we discard the data from one minute before and one minute after each mass switching event, and only retain the stable 3-minute data in the middle of each mass segment for analysis.

(2) Correction of multiple charge. The CPMA selects aerosol particles based on the balance between the centrifugal force and the electric field force,

$$\frac{M_p}{N_q} = \frac{eV}{r^2\omega^2 \ln(r_0/r_1)} \quad (1)$$

where M_p is the particle mass, N_q is the charge on each particle, e is the is the elementary charge (1.6×10^{-19}C), r_0 and r_1 are the radii of the inner and outer cylinders, and r is the center radius of the two cylinders, ω is the angular velocity at this radius.

When CPMA selected large mass aerosols with multiple charges, their mass-to-charge ratio may be similar to that of small mass aerosols with a single charge. To eliminate these large and multiply charged particles, we apply a correction based on their scattering signals. First, we summary the probability distribution of the scattering signals for each mass bin, and further fit the distribution to identify multiply charged particles with larger scattering signals. Only the singly charged particles was retained (Fig. S10c and d). The three-dimensional M_c-M_p distribution before and after correction is also shown in Fig. S10a and b. The scattering signals are fitted using the LEO method.

The charging ability of aerosols decreases with the reduction in particle size. This study is based on the method of limiting spheres developed by Fuchs et al. (1962), and uses convective diffusion and kinetic models to calculate the particle migration rates. Subsequently, the proportion of aerosols with a single charge in each size bin is assessed, with the particle density based on measurements by Zhao et al. (2019) in the field environment. The calculation results are shown in Fig. S11. Based on this, the total number of particles for each mass at different sizes is further obtained.

(3) Correction of collection efficiency.

The correction of sampling efficiency includes detector counting efficiency and tube losses. Before sampling, we measured the detection efficiency of the SP2 detector. The results showed that the counting concentrations of BC particles measured by the SP2 and CPC were generally consistent across different particle sizes. Therefore, this study assumes the counting efficiency of the SP2 detector to be 100%.

Due to Brownian motion, particles with smaller diameters tend to diffuse from regions of high concentration to regions of low concentration and deposit on the inner walls of the tube. In a tube where gas flows under laminar conditions, the particle

transmission efficiency η is related to the parameter $\zeta = \frac{\pi DL}{Q}$, where D represents the particle diffusion coefficient, L is the tube length, and Q is the volumetric flow rate of the gas. A mathematical expression was raised to characterize the transmission efficiency of particle deposition under laminar flow conditions (Gormley and Kennedy, 1984).

$$\eta = 1 - 2.56\zeta^{\frac{2}{3}} + 1.2\zeta + 0.177\zeta^{\frac{4}{3}} \quad \zeta < 0.009 \tag{2}$$

$$\eta = 0.819\exp(-3.657\zeta) + 0.097\exp(-22.3\zeta) + 0.032\exp(-57\zeta) \quad \zeta > 0.009 \tag{3}$$

According to Equations 2 and 3, the particle transmission efficiency of each M_p bins was showed in Fig. S11a.

Table S1. The M_R determination range of "transition-state" BC-containing particles at different periods

M_p (fg)	List	Case1	Case2	Case3
2.02	Transition Start	1.5	1.1	1.3
	Transition End	—	—	3.1
2.97	Transition Start	1.9	1.3	1.3
	Transition End	—	—	4.5
4.35	Transition Start	1.7	1.5	1.3
	Transition End	6.2	3.7	4.1
6.39	Transition Start	1.9	1.5	1.4
	Transition End	5.9	4.2	3.9
9.38	Transition Start	1.9	1.6	1.7
	Transition End	6.4	3.1	4.7
13.77	Transition Start	1.8	1.6	1.7
	Transition End	6.7	3.9	4.6
20.22	Transition Start	1.7	—	—
	Transition End	6.5	4.0	4.4
Average	Transition Start	1.78	1.43	1.45
	Transition End	6.34	3.78	4.19

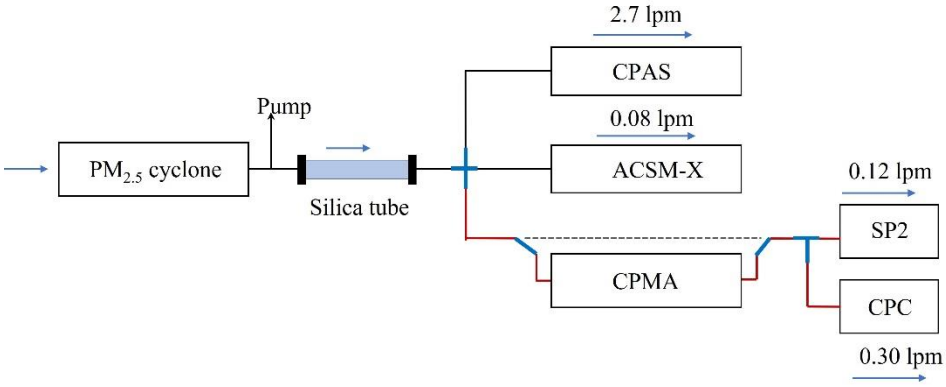

Figure S1. Schematic of the sampling system. The dotted line represents the SP2 sample flow, and the red line represents the CPMA-SP2 tandem system sample flow.

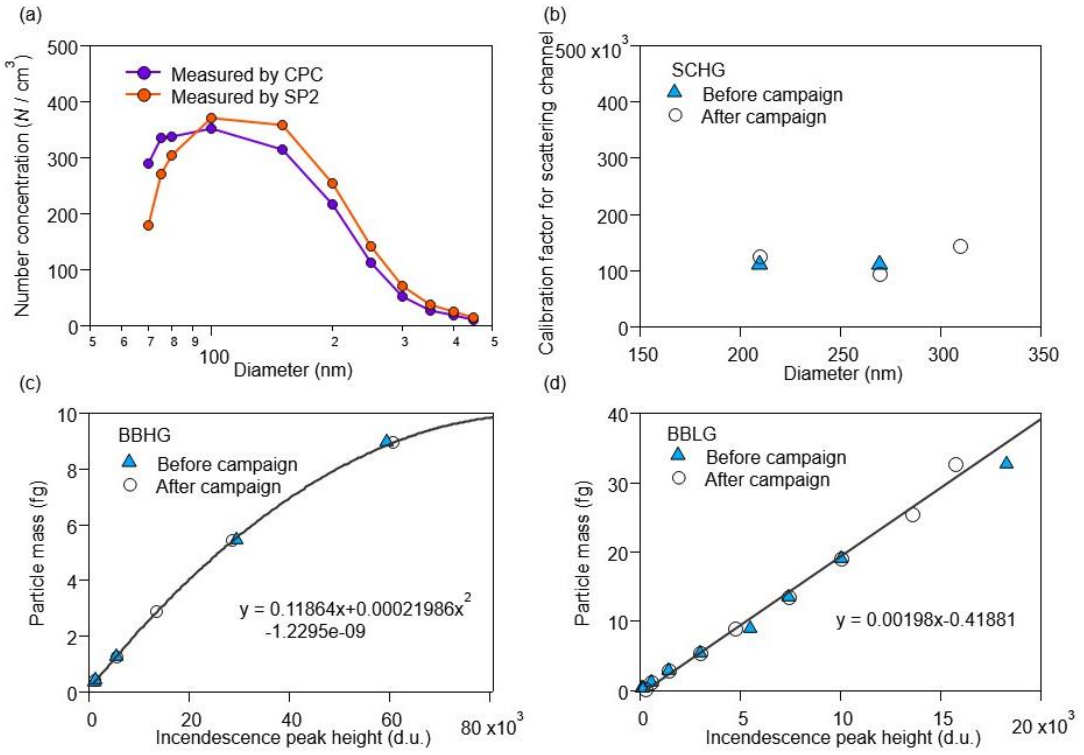

Figure S2. The number concentration measured by SP2 and CPC after DMA classification of size-resolved Aquadag aerosols (a). (b) showed the calibration factor for scattering channel before and after campaign. (c) and (d) display the correlation between incandescence peak height and BC particle mass at broadband high-gain and low-gain channel, respectively.

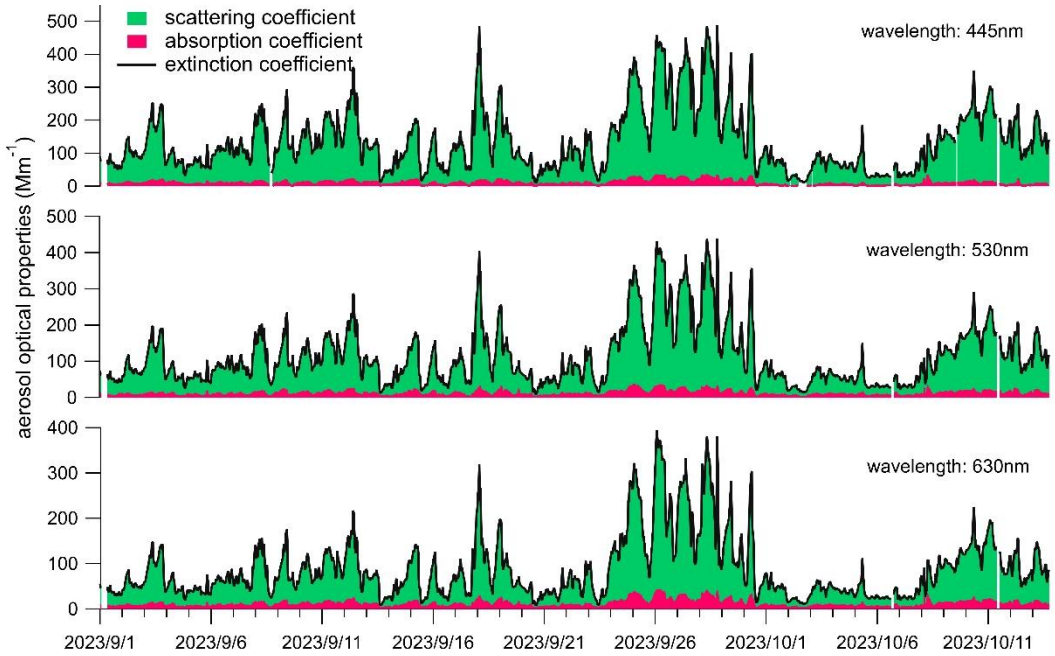

Figure S3. The scattering coefficient, absorption coefficient and extinction coefficient of particles were measured by CAPS at wavelength of 445 nm, 530 nm and 630 nm.

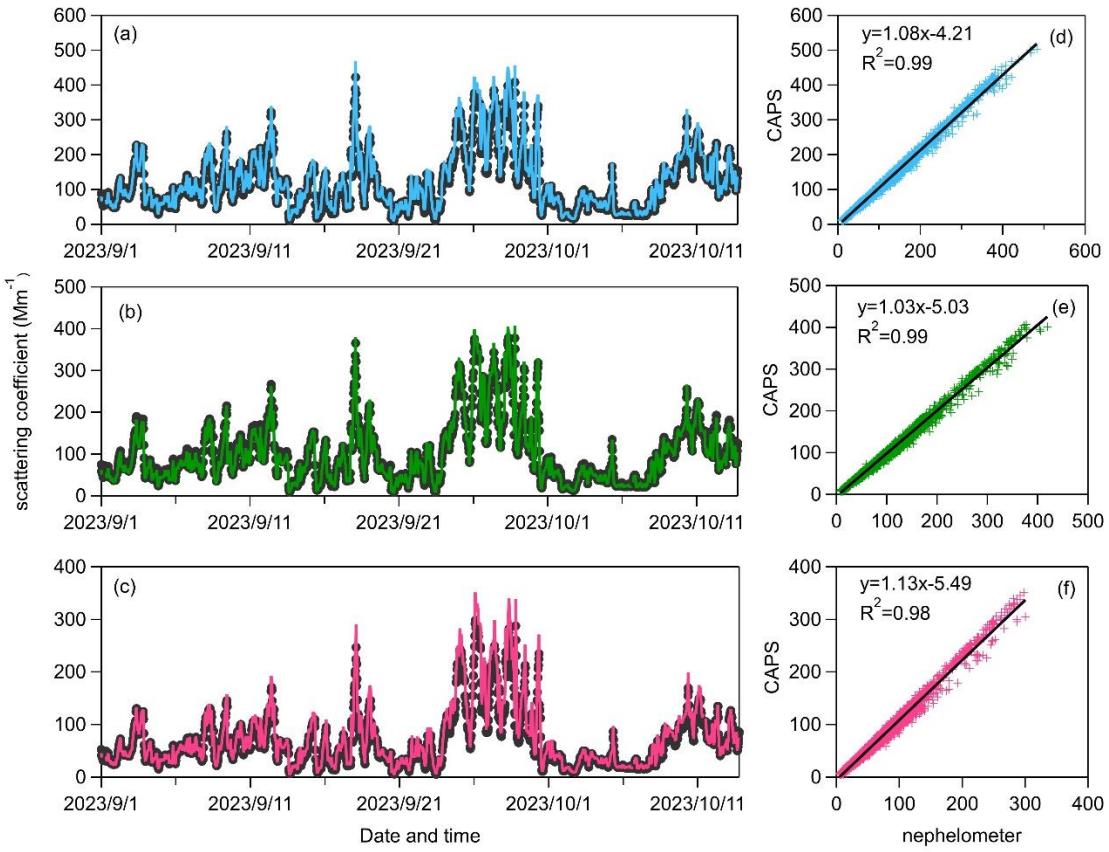

Figure S4. Comparisons of the scattering coefficients measured by CAPS at wavelengths of 445 nm, 530 nm, and 630 nm, and by the nephelometer at wavelengths of 450 nm, 525 nm, and 635 nm.

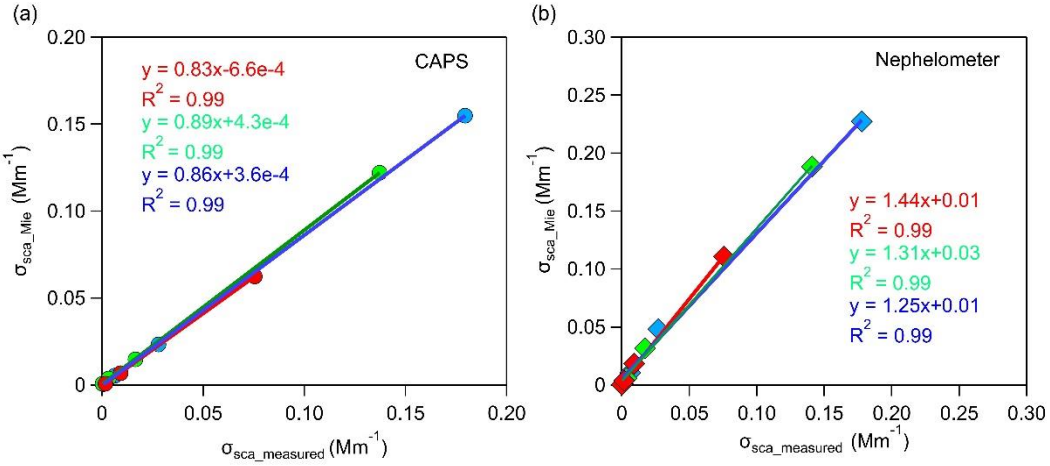

Figure S5. The scattering coefficients measured by CAPS (a) and the Nephelometer (b) are compared with those modeled using Mie theory.

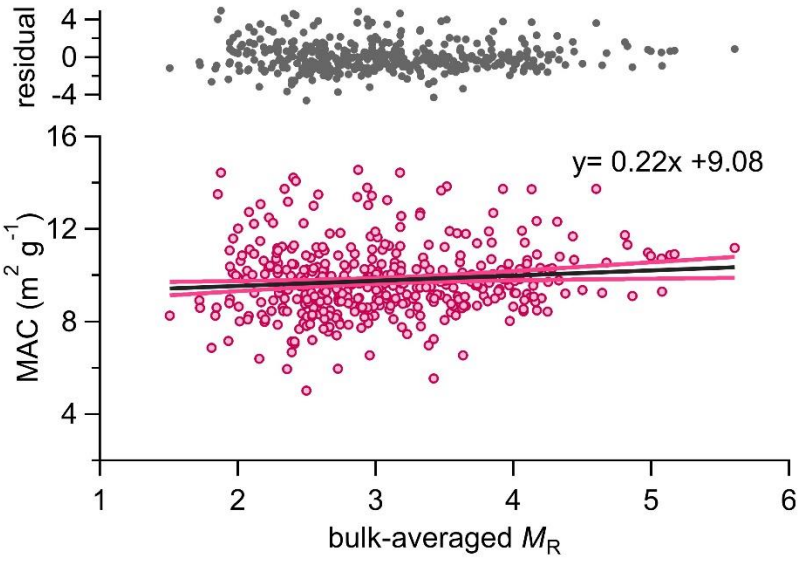

Figure S6. The relationship between MAC and bulk-averaged M_R at λ=630 nm is shown, with fitted lines and their associated 90th confidence intervals. The extrapolated MAC value for pure BC (MAC_{BC_core}) at a bulk-averaged M_R of 0 is 9.08 m^2 g^{-1} (630 nm), with uncertainties representing the 90th confidence level. The grey dots were the residual from the fits.

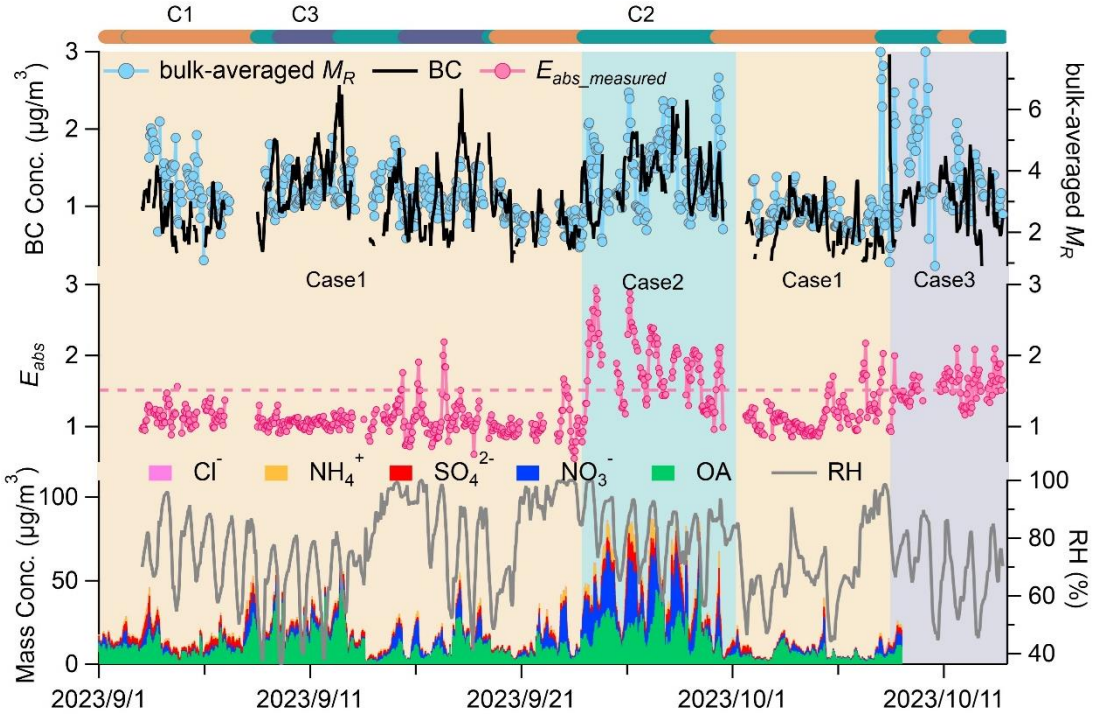

Figure S7. The time series of BC concentrations, bulk-averaged M_R, and the measured E_{abs}, and the chemical components including organic, nitrate, sulfate, ammonium, chloride and the relatively humidity (RH). Shaded regions indicate different cases: light yellow for Case 1, blue-green for Case 2, and gray for Case 3. The top horizontal bar indicates the air mass origins throughout the observation period; the associated air mass directions are illustrated in Fig. S8.

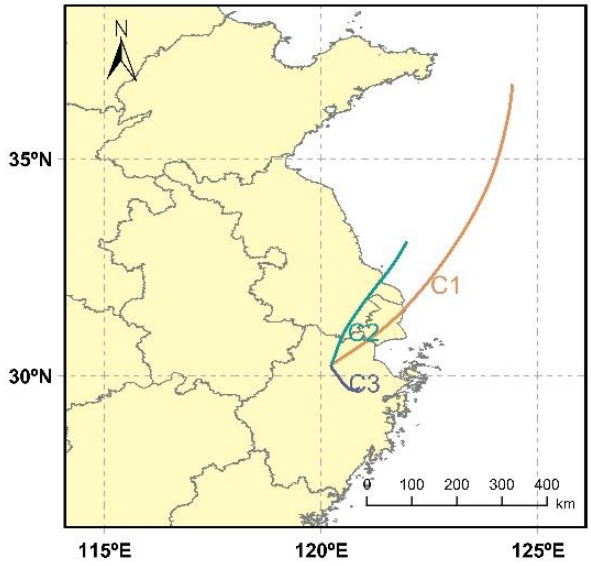

Figure S8. Air mass backward trajectory by during the observation period.

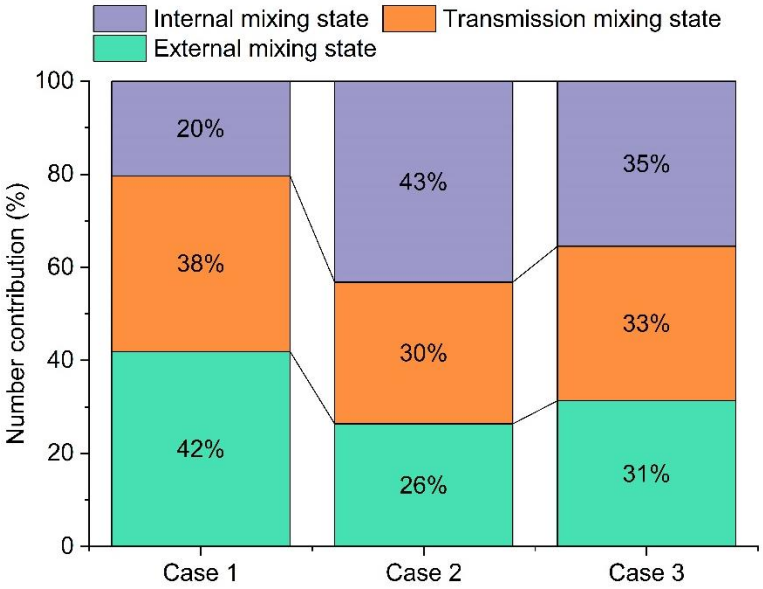

Figure S9. The proportions of externally mixed, transitional, and internally mixed BC-containing particles during different cases.

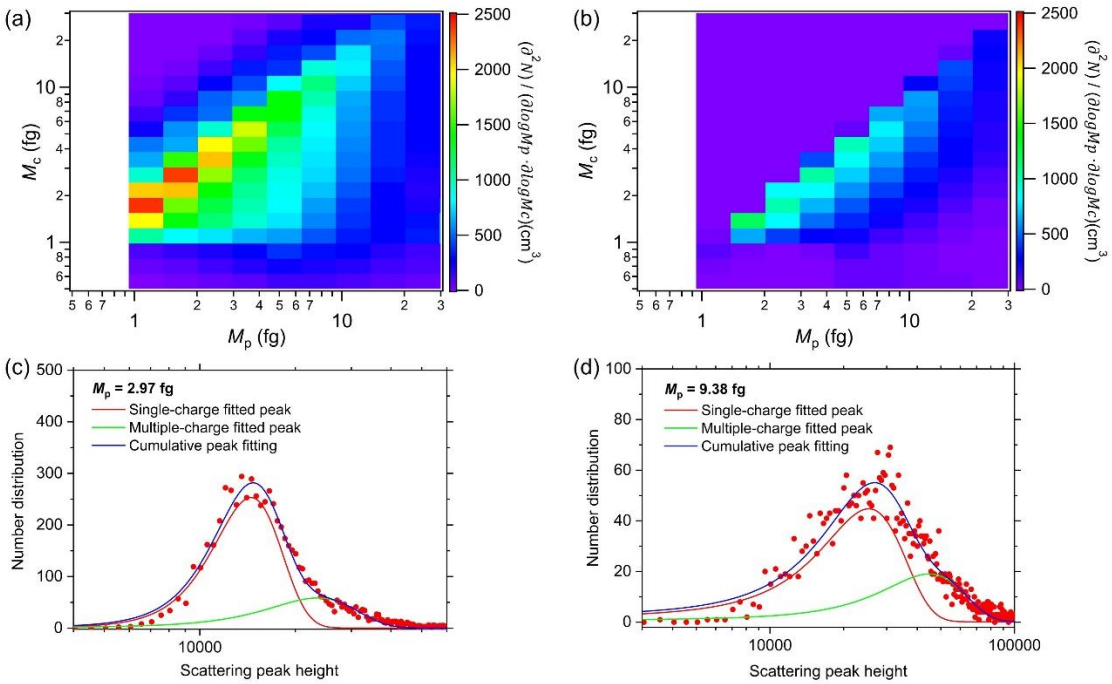

Figure S10. Multiple charging diagnostics in the tandem CPMA-SP2 system. (a) presents the number distribution of M_c-M_p before removing the BC-containing particles affected by multiple charging. (b) displays the number distribution of M_c-M_p after removing the BC-containing particles affected by multiple charging. (c) and (d) demonstrate the selection approach for single-charged BC-containing particles at different M_p, exemplified by M_p =2.97 fg and M_p =9.38fg.

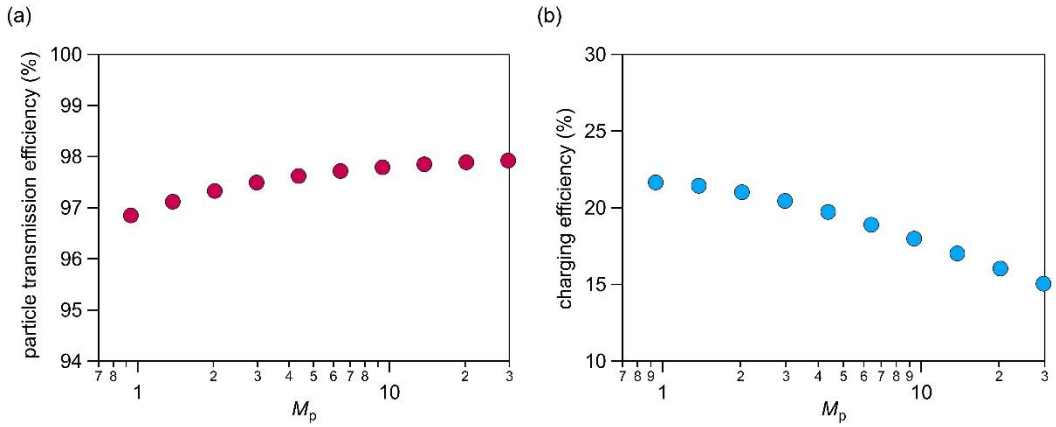

Figure S11. Mass-dependent charging efficiency of singly charged BC-containing particles and the associated tubing loss.

References:

Fuchs, N. A., Stechkina, I. B., and Starosselskii, V. I. (1962). On the determination of particle size distribution in polydisperse aerosols by the diffusion method. *British journal of applied physics*, *13*, 280-281. https://doi.org/10.1088/0508-3443/13/6/307

Gormley, P. G., and Kennedy, M. (1984), Diffusion from a Stream Flowing through a Cylindrical Tube, Proc. R. Ir. Acad., Sect. A. 52, 163-169.

Zhao, G., Tan, T., Zhao, W., Guo, S., Tian, P., and Zhao, C. (2019). A new parameterization scheme for the real part of the ambient urban aerosol refractive index. *Atmospheric Chemistry and Physics*, *19*(20), 12875-12885. https://doi.org/10.5194/acp-19-12875-2019